

Flux Contribution and Geometry of the Charge Exchange Emission in the Starburst Galaxy M82

HIROMICHI OKON,¹ RANDALL K. SMITH,¹ ADRIEN PICQUENOT,^{2,3,4} AND ADAM R. FOSTER¹

¹*Harvard-Smithsonian Center for Astrophysics, 60 Garden Street, Cambridge, MA 02138, USA*

²*Department of Astronomy, University of Maryland, College Park, MD 20742, USA*

³*X-ray Astrophysics Laboratory NASA/GSFC, Greenbelt, MD 20771, USA*

⁴*Center for Research and Exploration in Space Science and Technology, NASA/GSFC, Greenbelt, MD 20771, USA*

Submitted to ApJ

ABSTRACT

Recent X-ray studies of starburst galaxies have found that Charge eXchange (CX) commonly occurs between the outflowing hot plasma and cold gas, possibly from swept-up clouds. However, the total CX flux and the regions where CX occurs have been poorly understood. We present an analysis of the *XMM-Newton* observations of M82, a prototype starburst galaxy, aiming to investigate these key properties of the CX emission. We have used a blind source separation method in the image analysis with the CCD data which identified a component with the enhanced O-K lines expected from the CX process. Analyzing the RGS spectra from the region identified by the image analysis, we have detected a high forbidden-to-resonance ratio in the O VII He α triplet as well as several emission lines from K-shell transitions of C, N, and O enhanced in the CX process. The CX is less responsible for the emission line of Ne and Mg and the accurate estimation of the CX contribution is confirmed to be crucial in measuring chemical abundances. The temperature of the plasma as electron receiver in the CX process is significantly lower compared to that of the plasma components responsible for most of the X-rays. From the low temperature and an estimation of the CX emitting volume, we find that the CX primarily occurs in a limited region at the interface of the plasma and gas whose temperature rapidly decreases due to thermal conduction.

Keywords: galaxies: individual (M82) – galaxies: starburst – X-rays: galaxies

1. INTRODUCTION

Galaxy-scale outflows in starburst galaxies (Veilleux et al. 2005; Rubin et al. 2014) are responsible for removing energetic and chemically enriched materials from the galaxy, injecting them into the circumgalactic medium (CGM) or even the intergalactic medium (Werk et al. 2016; Borthakur et al. 2013). Such outflows regulate star formation activity within galaxies as well as act as the major driver of cosmic chemical enrichment (Peeples & Shankar 2011; Oppenheimer & Davé 2006). The prevailing picture is that outflows are formed by hot gas shock-heated by supernovae (SNe) and stellar winds that entrain dust and cold gas (e.g., Chevalier & Clegg 1985). X-ray emissions from the multi-phase gas have been widely used as diagnostics tools to investigate their kinematic and chemical properties (e.g., Tsuru et al. 2007; Lopez et al. 2020).

Detection of Charge eXchange (CX) based on recent observations of nearby starburst galaxies with RGS onboard *XMM-Newton* (Ranalli et al. 2008; Liu et al. 2011, 2012), gave us unique insights to the previous studies on outflows. CX is an atomic process predicted to occur between an ionized plasma and neutral matter in outflows (Lehnert et al. 1999; Lallement 2004), and selectively enhances several emission lines such as the forbidden (f) and resonance (r) in the O VII He α triplet. The measurements of the flux of the enhanced lines and their ratios allow us to put strong constraints on key parameters (e.g., bulk and turbulence velocities, and density) to understand complicated gas-phase physics (e.g., hydrodynamic effects such as shocks and turbulence, thermal conduction, and non-equilibrium emission processes) that play an important role of the evolution of outflows (e.g., Strickland & Heckman 2009). Although the number of results detecting CX emission in X-ray band is growing, its quantitative flux estimation and the investigation of the CX geometry have been poorly understood, as distinguishing thermal X-ray plasma and CX emission remains

difficult and the CX modeling is complex (e.g., Smith et al. 2014).

M82, the prototype of a starburst galaxy, is where CX emission was detected for the first time (Ranalli et al. 2008). Because of its proximity (3.6 Mpc Freedman et al. 1994) and large inclination angle ($i \sim 80^\circ$; McKeith et al. 1995), M82 is regarded as the ideal target for observational studies on outflows. Biconical outflows from the nuclear region of M82 extend perpendicularly to the galactic disc and their properties have been widely studied across the electromagnetic spectrum, tracing atomic H I and molecular gas (e.g., Walter et al. 2002; Salak et al. 2013), warm-ionized gas in H α (e.g., McKeith et al. 1995; Ohyama et al. 2002), hot plasma emitting X-rays (e.g., Watson et al. 1984; Lopez et al. 2020), and dust in the UV, IR, and submillimeter bands (e.g., Origlia et al. 2004; Hoopes et al. 2005). Past observations of M82 aiming to investigate the nature of X-rays pointed out the discrepancy between the plasma model and the CCD spectra in the O VII He α triplet in both the galactic disk and outflow regions of M82 (Konami et al. 2011; Lopez et al. 2020).

Here we report on an analysis of *XMM-Newton* data of M82, combining the application of a blind source separation method together with high resolution spectroscopy to pin down the origin of the CX emission. Throughout this paper, we adapt 3.6 Mpc as the distance to M82 (Freedman et al. 1994), and the statistical errors are quoted at the 1σ level.

2. OBSERVATIONS AND DATA REDUCTION

M82 has been observed with *XMM-Newton* many times between 2003 to 2021. In most of these observations, the field of view (FoV) of MOS and pn CCDs completely covers the entirety of M82 including both outflows. We used MOS and pn data only for the image analysis and identifying spectral characteristics. We reprocessed this data with the Science Analysis System software (SAS) version 19.1.0 and the Current Calibration Files, following the cookbook for analysis procedures of extended sources¹. We discarded short time Observation IDs whose MOS1+2 exposure time after the screening is less than 20 ks. The observations that meet the criteria are summarized in Table 1. Furthermore, two datasets (Obs. ID = 0870940101 and 0870940401) observed in the small window mode were not used. We used RGS data only for spectral analysis. These data were reprocessed using the `rgsproc` task in SAS. We extracted background light curves and filter out observation periods when the background count rate is higher than 0.15 cnt s^{-1} .

3. ANALYSIS AND RESULTS

3.1. Imaging Analysis

Our first purpose is to constrain the spatial distribution of a component with the enhanced O VII He α triplet expected from the CX process (e.g., Lallement 2004). We used a blind source separation method, the General Morphological Components Analysis (GMCA) (Bobin et al. 2015), that was designed specifically for cosmic microwave background reconstruction using *Planck* data. The method was recently introduced to an analysis of *Chandra* data by Picquenot et al. (2019) and the authors demonstrated that this algorithm works as a powerful tool to isolate physically meaningful components in the data, and identify extraction regions of interest. In the case of M82, the observed X-rays arise from multi-temperature thermal plasmas (cold: $\sim 0.2 \text{ keV}$, medium hot: $\sim 0.5 \text{ keV}$, hot: $\sim 0.9 \text{ keV}$, and extreme hot: $\leq 6 \text{ keV}$) as well as nonthermal emission, in addition to the CX emission we are interested in (e.g., Konami et al. 2011; Lopez et al. 2020). Although the GMCA has no intrinsic knowledge of these different components, if the CX emission has an identifiable spectral and spatial shape in the data, it should be able to extract it.

The primary concept of the GMCA method is to take into account the morphological particularities of distinct components by measuring the sparsity level in the wavelet domain for each energy slice of a 3-D data cube of the photon position (x, y) and energy (E). Inputs to the algorithm are the data cube and the user-defined number N of components to extract, and the output is a set of N images associated with the spectra. In our analysis, the position (x, y) and energy (E) information in the cube correspond to the sky coordinate of each event on band images and the energy range we define, respectively. We used the data in the energy range from 0.3 keV to 2.5 keV where all CX-enhanced lines (e.g., C VI He γ : 0.459 keV; N VII Ly α : 0.500 keV... Si XIII He α f : 1.839 keV) discussed in previous work (e.g., Zhang et al. 2014) are covered, and generated 44 band images with `binning = 3` in equal 0.05 keV increments, with `adapt-merge`. Subsequently, we merged them together to build the input data cube. The number N was fixed to 4. For the case of $N \geq 5$, two of the components show similar images and spectra, which can be interpreted as the overfitting of the data. On the other hand, for $N \leq 3$, the CX component of interest and other components cannot be disentangled well.

Figure 1(a) shows the spectra of the primary extracted components. The spectrum of Component 1 is characterized by the soft emission below 1 keV including the O VII He α triplet selectively enhanced by the CX process as reported by previous work (e.g., Ranalli et al. 2008). In the spectrum of Component 2, one can see a strong Fe-L complex and Ne VIII Ly α lines. These characteristics are consistent with the interpretation that Component 2 mainly represents

¹ <https://heasarc.gsfc.nasa.gov/docs/xmm/esas/cookbook/xmm-esas.html>

Table 1. Observation log

Target	Obs. ID	Obs. Date	(R.A., Dec.) ^a	Roll angle (deg)	Effective Exposure (ks)		
					MOS ^b	pn	RGS
M82	0112290201	2001 May 6	(9 ^h 55 ^m 49 ^s .99, +69°40′45″.0)	293.0	46.7	18.0	24.7
M82	0206080101	2004 April 23	(9 ^h 55 ^m 52 ^s .20, +69°40′47″.0)	319.3	115.0	46.1	71.5
M82 ULX	0560590101	2008 October 3	(9 ^h 55 ^m 50 ^s .19, +69°40′47″.0)	138.3	52.3	28.1	30.9
M82 ULX	0560590201	2009 April 17	(9 ^h 55 ^m 50 ^s .19, +69°40′47″.0)	315.7	29.1	15.1	21.9
M82 ULX	0560590301	2009 April 29	(9 ^h 55 ^m 50 ^s .19, +69°40′47″.0)	295.9	33.0	13.4	30.1
M82 X-1	0657802101	2011 September 24	(9 ^h 55 ^m 49 ^s .91, +69°40′44″.4)	147.2	25.3	6.5	17.4
M82 X-1	0657802301	2011 November 21	(9 ^h 55 ^m 49 ^s .91, +69°40′44″.4)	100.3	20.8	9.2	18.7
M82 X-2	0870940101	2021 April 16	(9 ^h 55 ^m 51 ^s .03, +69°40′45″.0)	312.6	41.8	–	27.2
M82 X-2	0870940401	2021 April 16	(9 ^h 55 ^m 51 ^s .03, +69°40′45″.0)	304.8	60.0	25.1	31.9

^aEquinox in J2000.0.

^bThe total effective exposure of MOS 1 and MOS 2.

thermal emission from moderately hot plasma ($kT_e \sim 0.5$ – 1.0 keV). The spectrum of Component 3 is described by a featureless spectral continuum dominant above ~ 2 keV. Given the count map as shown in Figure 1(b), Component 3 can be considered to be dominated by a nonthermal emission from M82 X-1 (Konami et al. 2011). Component 4 consists of a line-like structure at ~ 1.5 keV. The structure arises from a neutral Al line (1.49 keV) in the instrumental background (Kuntz & Snowden 2008) whose careful handling is often required in the analyses of diffuse sources (e.g., Okon et al. 2020, 2021).

3.2. CCD Spectral Characteristics

The spectral interpretations in §3.1 are, however, merely qualitative. To quantify these interpretations we used MOS1+2 spectra extracted from representative regions in Figure 1(d). Regions 1–3 are dominated by GMCA components 1–3 based on the fraction map in Figure 1(c), defined as $f_i = N_i / \sum_{i=1-4} N_i$, where N_i is the number of photons in the count map for the component i in Figure 1(b). We found that the MOS spectrum from Region 1 exhibit the strong O VII He α and O VIII Ly α lines expected from the GMCA results (Figure 2). We also confirmed that the enhanced Fe-L complex and Ne IX Ly α from a hot thermal plasma is seen in spectra from Regions 2 and that a nonthermal continuum above 2 keV dominates the spectrum from Region 3.

3.3. RGS Spectral Analysis

Unfortunately, CCDs cannot spectrally-resolve the O VII triplet to detect conclusive evidence of CX via a significantly high f/r ratio. We therefore turned to RGS spectra. Given the deviation of the wavelength of the incident photon

against its off-axis angle², the difference of the center energy of the O VII f and r corresponds to the source size of $\sim 4'$. We focused on a bright peak with an angular diameter $\sim 2'$ enough to resolve the multiplet lines, in the south outflow as shown in the map of Component 1 (noted as “Peak” in Figure 3(a)). We used all data sets in which the RGS FoVs completely cover the Peak region regardless of the roll angle (Obs. ID=0112290201, 0206080101, 0560590201, 0560590301, 0870940101, 0870940401). Figure 3(b) shows the first- and second-order spectra of the Peak region, where the data from all the observations are integrated to improve the photon statistics. The f and r line in the RGS data are clearly resolved and the high f/r ratio is confirmed.

We first measured the line intensity of the O VII He α f and r lines, as well as O VIII Ly α since their ratios offer helpful guides in complex CX modeling. Given the variation in the roll angle among the datasets, we independently fitted RGS1+2 first-order spectra in the energy band of 0.55–0.70 keV with a phenomenological model consisting of a bremsstrahlung continuum and five Gaussians accounting for O VII f (0.574 keV), intermediate (0.569 keV), and r (0.561 keV), O VIII Ly α (0.654 keV), and O VII Ly β lines (0.666 keV). The central energy of the Gaussian components was fixed to the corresponding line energy. The intensity of the Gaussians and the parameters concerning the continuum were allowed to vary. We convolved RGS response matrices (RMFs) with the spatial profile of source emission in the MOS+pn image in the 0.55–0.70 keV band, using the FT00L `fttrgsrmfsmooth`. In the spectral fitting, we used XSPEC software version 12.11.1 (Arnaud 1996) and

² <https://heasarc.gsfc.nasa.gov/docs/xmm/esas/cookbook/xmm-esas.html>

Table 2. The intensities of the O and Ne emission.

Obs. ID	O <i>f</i> ^a	O <i>r</i> ^a	O Ly α ^a	O <i>f</i> /O <i>r</i>	Ne <i>f</i>
0112290201	1.08 ^{+0.18} _{-0.17}	0.62 ^{+0.17} _{-0.16}	3.12 \pm 0.15	1.73 ^{+0.64} _{-0.43}	0.63 \pm 0.10
0206080101	0.91 \pm 0.09	0.51 ^{+0.09} _{-0.08}	3.05 \pm 0.10	1.78 ^{+0.57} _{-0.41}	0.93 \pm 0.08
0560590201	0.84 ^{+0.14} _{-0.13}	0.47 ^{+0.12} _{-0.19}	2.52 ^{+0.19} _{-0.13}	1.79 ^{+0.63} _{-0.59}	0.66 \pm 0.12
0560590301	0.98 \pm 0.20	0.54 ^{+0.21} _{-0.18}	2.88 \pm 0.21	1.81 ^{+0.71} _{-0.42}	0.71 \pm 0.10
0870940101	0.83 ^{+0.16} _{-0.15}	0.46 ^{+0.15} _{-0.14}	2.17 \pm 0.13	1.80 ^{+0.78} _{-0.51}	0.70 \pm 0.10
0870940401	0.77 ^{+0.16} _{-0.15}	0.40 ^{+0.15} _{-0.14}	2.45 ^{+0.14} _{-0.13}	1.93 ^{+0.65} _{-0.44}	0.79 \pm 0.12
Exposure Weighted	0.90 \pm 0.14	0.50 \pm 0.14	2.77 ^{+0.15} _{-0.14}	1.80 ^{+0.65} _{-0.45}	0.79 \pm 0.10

^aIn units of 10^{-4} photons $\text{cm}^{-2} \text{s}^{-1}$.

the *C*-statistic (Cash 1979) on unbinned spectra. The results are summarized in Table 2. Finally, we calculated the exposure-weighted mean intensity I and the statistical error $\sigma_{I,\text{stat}}$ among the measurements as follows,

$$I = \frac{\sum_i I_i \times t_i}{\sum_i t_i}, \quad (1)$$

$$\sigma_{I,\text{stat}} = \sqrt{\frac{\sum_i \sigma_{I_i,\text{stat}}^2 \times t_i}{\sum_i t_i}} \quad (2)$$

where I_i , $\sigma_{I_i,\text{stat}}$, and t_i are the intensity, statistical error, and exposure time of the observation i , respectively.

Figure 4(a) compares the measured O VII He α *f/r* ratio with theoretically expected curves from plasma and CX models computed with PyatomDB³ and the AtomDB CX package⁴ based on cross sections from the Kronos database (Mullen et al. 2016, 2017; Cumbee et al. 2018), respectively. Here, we presented three cases of the CX process where the collision velocity between the plasma and gas is 500 km/s, 1000 km/s or 1500 km/s, taking into account the velocity of outflow plasma estimated with the Chevalier & Clegg (1985) model \sim 1000–2500 km/s (Strickland & Heckman 2009) and the observed H α clump \sim 600 km/s (Shopbell & Bland-Hawthorn 1998). We found that the observed *f/r* ratio requires a large CX contribution (\gtrsim 50 %) for the O He α *f* if the CX is assumed to occur between the gas and a hot plasma whose temperature kT_e is \sim 0.2 keV, \sim 0.5 keV, or \sim 0.9 keV reported by previous work (Konami et al. 2011; Lopez et al. 2020). In Figure 4(b), we plotted the observed flux of O Ly α overlaid with the expected flux level assuming that CX is responsible for 50% of the total flux of O VII He α *f*. This comparison requires an upper limit for $kT_{e,\text{CX}} \sim$ 0.35 keV for the plasma component receiving electrons via CX, regardless of the collision velocity. In following spectral analysis, we thus assume that CX

occurs between the gas and the coldest plasma component with $kT_e \sim$ 0.2 keV.

Based on this assumption, we fitted the RGS first- and second-order spectra. We employed `bvapec` implemented in XSPEC to describe the multiple collisional ionization equilibrium plasma components (hot: $kT_{e,\text{hot}} \sim$ 0.9 keV; medium hot: $kT_{e,\text{med}} \sim$ 0.5 keV; cold: $kT_{e,\text{cold}} \sim$ 0.2 keV). To model the CX emission, we used ACX2⁵ where the CX temperature $kT_{e,\text{CX}}$ is linked to electron temperature $kT_{e,\text{cold}}$ in the cold plasma. ACX2 includes any velocity-dependent effects for the calculation of cross section not included in the previous ACX model. The collision velocity v_{col} in ACX2 cannot be constrained and does not significantly affect the final results, so we fix v_{col} at 1000 km/s. We set the (n, l) distribution⁶ of the exchanged ions to the default value 8, and assumed the case that one ion repeatedly captures electrons until it becomes neutral, which is available in the current CX model. The electron temperature of the plasma components and the normalization of the plasma and CX components were allowed to vary. We tied the abundances of C, N, O, Fe, and Ni among both the components and let them vary. The abundances of metals with line emission not detected were fixed to 1 solar. For the intrinsic absorption for M82 ($N_{\text{H},\text{M82}}$) and the galactic absorption ($N_{\text{H},\text{MW}}$) in the direction toward M82, we used TBabs with solar abundances (Wilms et al. 2000) and TBvarabs with the metal abundances in Origlia et al. (2004), respectively. The hydrogen column density $N_{\text{H},\text{M82}}$ of the former was fixed to $0.4 \times 10^{21} \text{ cm}^{-2}$ (Dickey & Lockman 1990), whereas that of the latter was left as a free parameter. In addition to these models, we added a power law to account for nonthermal emission from M82 X-1. The photon index Γ was fixed at 0.55 given by Konami et al. (2011) whereas the normalization was left free. To account for the variation of the flux profile with energy range, we applied different

³ <https://atomdb.readthedocs.io/en/master/>

⁴ <https://github.com/AtomDB/ACX2>

⁵ <https://github.com/AtomDB/ACX2>

⁶ <https://github.com/AtomDB/ACX2/blob/master/pdf/acx2.pdf>

Table 3. Best-fit model parameters of the spectra of the all observation.

Model Function	Parameters	Obs. ID					
		0112290201	0206080101	0560590201	0560590301	0870940101	0870940401
TBabs	$N_{\text{H,MW}}$ (10^{21} cm^{-2})	= 0.4 (fixed)					
TBvarabs	$N_{\text{H,M82}}$ (10^{21} cm^{-2})	0.8 ± 0.2	1.78 ± 0.07	0.6 ± 0.2	1.0 ± 0.1	0.9 ± 0.1	1.2 ± 0.1
VACX2	$kT_{e,\text{CX}}$ (keV)	= $kT_{e,\text{cold}}$					
	Z_{C} (Solar)	2.6 ± 0.5	1.8 ± 0.3	0.8 ± 0.3	2.7 ± 0.5	1.1 ± 0.3	1.6 ± 0.5
	Z_{N} (Solar)	0.8 ± 0.2	$0.79^{+0.07}_{-0.06}$	0.6 ± 0.2	0.9 ± 0.1	0.8 ± 0.1	0.8 ± 0.1
	Z_{O} (Solar)	0.42 ± 0.06	0.38 ± 0.01	0.34 ± 0.03	0.43 ± 0.03	0.37 ± 0.02	0.42 ± 0.03
	Z_{Ne} (Solar)	1.1 ± 0.3	0.99 ± 0.06	1.1 ± 0.2	1.2 ± 0.1	1.1 ± 0.1	1.2 ± 0.1
	Z_{Fe} (Solar)	$0.40^{+0.05}_{-0.06}$	0.37 ± 0.03	0.26 ± 0.04	$0.35^{+0.04}_{-0.03}$	0.28 ± 0.03	0.31 ± 0.03
	Z_{Ni} (Solar)	0.9 ± 0.3	0.9 ± 0.1	0.7 ± 0.3	0.9 ± 0.2	0.6 ± 0.3	0.8 ± 0.3
	v_{col} (km/s)	1000 (fixed)					
	VEM_{CX}^a (10^{57} cm^{-5})	0.5 ± 0.2	1.5 ± 0.3	0.6 ± 0.2	0.7 ± 0.2	0.6 ± 0.2	0.7 ± 0.2
bvapec	$kT_{e,\text{cold}}$ (keV)	0.22 ± 0.02	0.21 ± 0.01	0.22 ± 0.02	0.20 ± 0.02	0.20 ± 0.02	0.22 ± 0.02
	Abundance	= Abundances of the ACX component					
	σ_{cold} (km/s)	0 (fixed)					
	v_{cold} (km/s)	0 (fixed)					
	$\text{VEM}_{\text{cold}}^b$ (10^{61} cm^{-5})	≤ 0.7	≤ 0.9	≤ 0.6	≤ 0.6	≤ 0.5	≤ 0.5
bvapec	$kT_{e,\text{med}}$ (keV)	0.44 ± 0.01	0.419 ± 0.006	0.44 ± 0.02	0.45 ± 0.01	0.44 ± 0.01	0.41 ± 0.01
	Abundance	= Abundances of the ACX component					
	σ_{med} (km/s)	≤ 558	796^{+173}_{-184}	581^{+157}_{-149}	345^{+63}_{-61}	1183^{+163}_{-212}	858^{+179}_{-176}
	v_{med} (km/s)	313^{+46}_{-44}	320^{+60}_{-66}	260^{+118}_{-106}	261^{+128}_{-129}	1046^{+138}_{-168}	970^{+168}_{-170}
	$\text{VEM}_{\text{med}}^b$ (10^{61} cm^{-5})	2.9 ± 0.5	5.4 ± 0.4	2.9 ± 0.5	3.8 ± 0.4	$3.3^{+0.6}_{-0.5}$	3.2 ± 0.5
bvapec	$kT_{e,\text{hot}}$ (keV)	0.85 ± 0.03	0.82 ± 0.01	0.89 ± 0.03	0.91 ± 0.02	0.81 ± 0.03	0.79 ± 0.03
	Abundance	= Abundances of the ACX component					
	σ_{hot} (km/s)	≤ 2149	122^{+23}_{-41}	2061^{+527}_{-630}	799^{+258}_{-267}	≤ 1429	≤ 891
	v_{hot} (km/s)	670^{+273}_{-277}	-114^{+92}_{-95}	1004^{+340}_{-312}	≤ 900	189^{+172}_{-169}	99^{+153}_{-161}
	$\text{VEM}_{\text{hot}}^b$ (10^{61} cm^{-5})	2.2 ± 0.3	4.6 ± 0.3	3.5 ± 0.5	$2.6^{+0.2}_{-0.3}$	$2.6^{+0.4}_{-0.3}$	3.1 ± 0.4
power law	Γ	0.55 (fixed)					
	Norm ^c	0.8 ± 0.1	1.33 ± 0.07	0.7 ± 0.1	1.2 ± 0.1	0.6 ± 0.1	0.7 ± 0.1
	C-stat / d.o.f.	3986 / 3261	4153 / 3252	2990 / 3252	4093 / 3252	3867 / 3252	3846 / 3252

^aThe volume emission measure integrated over the line of sight, i.e., $\int n_e n_{(\text{H+He})} dV$.

^bThe volume emission measure integrated over the line of sight, i.e., $\int n_e n_{\text{H}} dV$.

^cThe unit is 10^{-4} photons / keV / cm^2/s at 1 keV

5 RMFs convolved with the five energy band images of 0.45–0.60 keV, 0.60–0.70 keV, 0.70–0.85 keV, and 0.85–1.25 keV. We did not use the spectra of the energy band above 1.25 keV as the significant difference of the profiles of the thermal and nonthermal emission creates a large uncertainty in the RMFs. This modeling gives good fits, as shown in Figure 5. The best-fit parameters are summarized in Table 3.

4. DISCUSSION

4.1. CX contribution

We have applied the GMCA method to the CCD data of the XMM observations of M82, and for the first time constrained the location of the component with enhanced CX emission in the starburst galaxy. Analyzing the RGS spectra from the Peak region in the south outflow, we have detected unusually high O VII He α f/r ratio as well as clearly resolved emission lines selectively enhanced in the CX process such as C VI K γ , N VII Ly α , and O VIII Ly α . The high ratio and the presence of line emission using parts of the RGS we used have been previously discussed (e.g., Liu et al. 2011; Zhang et al. 2014). Our results confirm their conclusion and

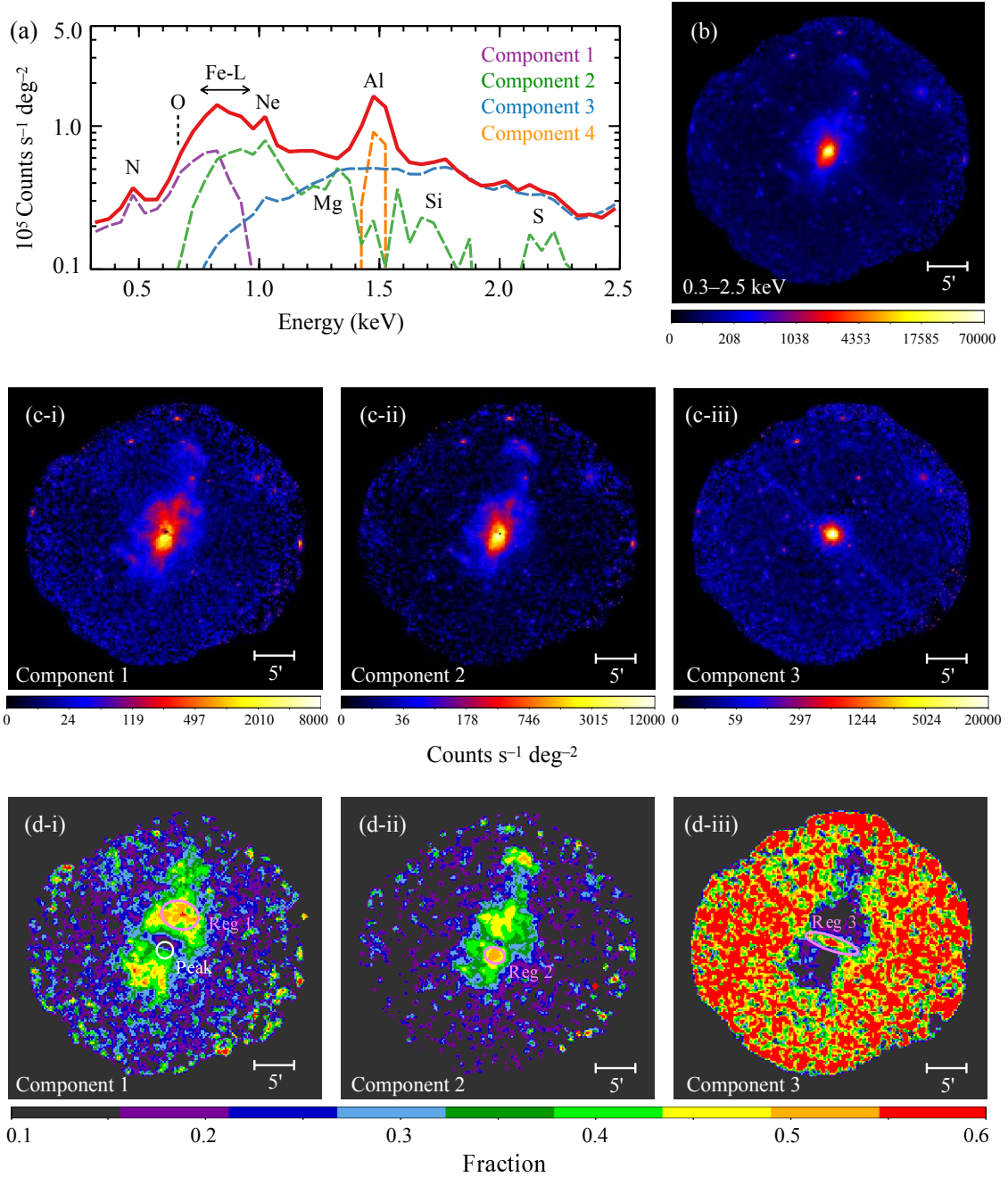


Figure 1. Results of the GMCA analysis applied to the M82. (a) Output spectra of the four components. Components 1 (purple), 2 (green), 3 (blue), and 4 (orange) predominantly consist of CX, hot plasma, nonthermal emission, and line emission due to detector background, respectively. The input data before the component extraction (red) is given by the sum of the components. Counts maps of (b) the input and (c-i)-(c-iii) the components. (d-i)-(d-iii) Fraction of each component, defined as $f_i = N_i / \sum_{i=1-4} N_i$, where N_i is the number of photons in the corresponding count map. The regions enclosed by the magenta lines in panel (d) are the three representative regions whose spectra are plotted in Figure 2. The white circle indicates the Peak region as shown in Figures 3(a).

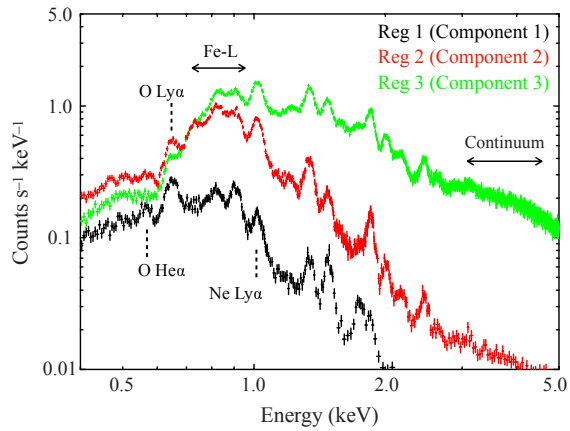


Figure 2. MOS1+2 spectra extracted from the representative region 1 (black), 2 (red), and 3 (green) in Figure 1(c).

indicate that the CX emission accounts for $\sim 50\%$, $\sim 30\%$, $\sim 60\%$, $\sim 40\%$, and $\sim 30\%$ of the total flux of the C VI K γ , N VII Ly α , O VII f , O VII r , and O VIII Ly α lines, respectively.

Some previous work (e.g., Zhang et al. 2014; Lopez et al. 2020) discussed the CX contribution in the Ne VII and Mg IX triplets in addition to the above line emission. For example, Zhang et al. (2014) claimed the CX is responsible for more than 30% of the total flux of Ne VII f although the contribution in our spectral fits is less than $\sim 10\%$. The discrepancy between these and our results arises from the selection of the recipient plasma in the CX modeling. Figure 6(a) shows the Ne f flux directly estimated with RGS data via the manner⁷ used in Suzuki et al. (2020) and the flux level expected the CX process as a function of the plasma temperature. In the flux calculation, we have assumed that 60% of the observed O VII f line is emitted in the CX process and computed the flux ratio of Ne IX f /O VII f with the same package in Sec 3.3 using the abundance ratio $Z_{\text{O}}/Z_{\text{Ne}} = 1.1/0.4$ from Table 2. The Ne f flux curve significantly varies with the plasma temperature since the population of H-like and bare ions that can emit the Ne f lines after the electron transfer is sensitive to the plasma temperature (Figure 6(b)). If we employ $kT_{e,\text{CX}} \sim 0.2$ keV as demonstrated in Sec 3.3, the CX contribution for the Ne f is less than $\sim 10\%$. On the other hand, Zhang et al. (2014) assume $kT_{e,\text{CX}}$ to be ~ 0.6 keV, suggesting the CX contribution is overestimated.

This change in the modeled CX emission implies that the abundance measurements in the hot plasmas must be updated as well. In Figure 7, we compare the obtained abundance pattern with that given by Zhang et al. (2014) and

⁷ To measure the Ne f and r flux, we delete the two transition in the XSPEC model package and perform the spectral fittings with the best-fit model in Table 3 plus additional Gaussians accounting for the two lines. Detailed procedures are described in Sec 5 in Suzuki et al. (2020)

Lopez et al. (2020). It is worth pointing out that overall our abundances tend to be lower except for carbon showing the opposite trend even if we consider their differences between observations. The cause of the abundance variations could be explained by the difference of the source regions due to the different roll angles and/or the position-to-position fluctuation of the column density, although it is hard to conclude it. A collection of Core Collapse (CC) events arising from star formation would naturally lead to super-solar abundance ratios of α elements versus Fe (e.g., Nomoto et al. 2006). Although the $[\text{Ne}/\text{Fe}] (= \log_{10}(Z_{\text{Ne}}/Z_{\text{Fe}})) \sim 0.51$ ratio remains high and consistent with typical nucleosynthesis models, the $[\text{O}/\text{Fe}] \sim 0.07$ is much smaller. Given that Origlia et al. (2004) reported high ratio of α elements including O to Fe with the near-infrared observations of stars and cold gas in the disc, the puzzling $[\text{O}/\text{Fe}]$ behavior should be interpreted as the result of significant O depletion rather than Fe enhancement. Some O might suffer severe dust depletion since CC supernovae produce the large amount of dust (e.g., Todini & Ferrara 2001). However, in the scenario, other elements are also expected to be depleted (e.g., Savage & Sembach 1996; Boogert et al. 2015) so that it is needed to confirm if the observed abundance pattern can be explained by the model including dust evolution. An alternative possibility is the uncertainty due to the modeling (e.g., are abundances the same among the three plasma and CX components? or are $kT_{e,\text{CX}}$ and $kT_{e,\text{cold}}$ really the same?). In either case, follow-up observation with micro-calorimeters onboard future satellites such as XRISM, will offer better understanding of the chemical property of the starburst galaxy.

4.2. CX geometry

The maps of the three components extracted in the GMCA analysis and their comparison with the gas distribution provides an unbiased look at the geometry of the CX component of the galaxy. Figure 8 shows the location of each component overlaid on the H α image with the Advanced Camera for Surveys (ACS) onboard the Hubble Space Telescope (HST) (Mutchler et al. 2007). We find Component 1 with enhanced CX emission to be spatially coincident with the distribution of the H α filaments extending in both north and south sides of the galactic disk. Numerical (e.g., Cooper et al. 2008) and hydrodynamical simulations (e.g., Melioli et al. 2013; Schneider et al. 2020) show that these vast H α structures are created by swept-up gas that has been dragged by plasma outflows. Our results support the idea that the CX process occurs at the interface between the plasma and gas components within outflow; similar conclusions were reached by Lallement (2004) and Wu et al. (2020) from numerical simulations.

Another clue to the CX geometry comes from the fraction of the CX emitting volume V_{CX} with respect to the outflow

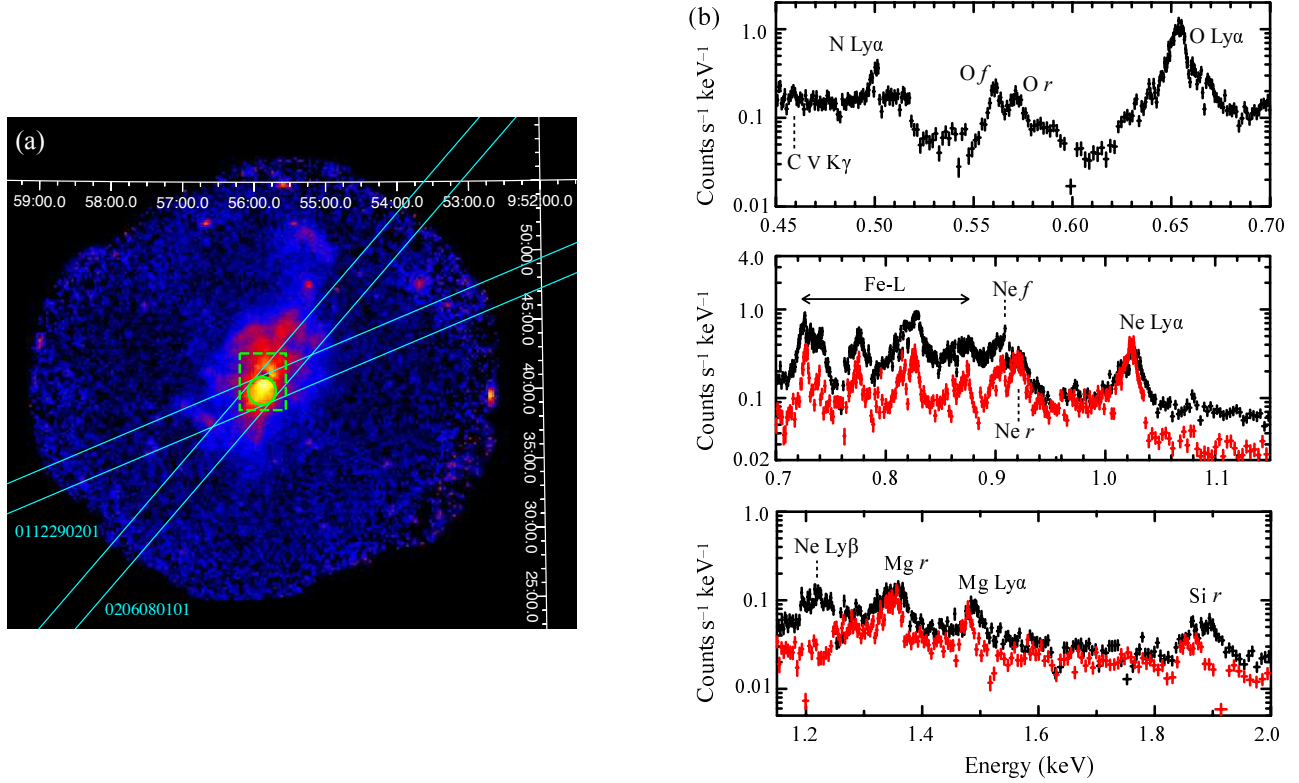


Figure 3. (a) Same as Figure 1(b-i) but we show the location of Peak region (green circle) and RGS spectral extraction regions (cyan) of OBS. ID=0112290201 and 0206080101 whose the roll angles are the maximum and minimum, respectively. The green box displays the area of Figure 7. (b) RGS1+2 first- (black) and second-order (red) spectra where all used data sets are integrated.

volume V_{pl} . We can estimate V_{CX} to be $3.6 \times 10^{56} \text{ cm}^3$ (see Appendix A), while $V_{\text{pl}} \sim 2.1 \times 10^{65} \text{ cm}^3$ assuming the morphology to be a cylinder with a radius of 1 kpc ($= 1'$) and a height of 2 kpc ($= 2'$). The fraction $\sim 10^{-9}$ is significantly smaller than the typical filling factor of the clouds within outflow ($0.001 - 0.1$; Müller-Sánchez et al. 2013; Sharp & Bland-Hawthorn 2010), indicating the CX occurs in an extremely limited region near the interface zone. This interpretation is indirectly supported by the fact that the temperature $kT_{e,\text{CX}} \sim 0.2 \text{ keV}$ of the plasma acting as an electron receiver for the CX process is much lower than the other plasma temperatures ($kT_{e,\text{med}} \sim 0.5 \text{ keV}$ and $kT_{e,\text{hot}} \sim 0.9 \text{ keV}$) which account for most of thermal X-rays. Neutral hydrogen, typically the major electron donor in the CX process, is easily ionized so that it cannot deeply penetrate into the hot plasma (e.g., Wise & Sarazin 1989). The low $kT_{e,\text{CX}}$ can be explained if the CX process mainly occurs in the layer with plasma temperature rapidly varying due to thermal conduction by the gas.

5. CONCLUSIONS

We have performed an analysis of X-ray emission of M82, a prototype starburst galaxy, obtained with *XMM-Newton* observations in order to investigate the CX flux contribution and its geometry. We have applied a blind source separation

method to the analysis of the CCD data and identified the spatial distribution of the component with the enhanced O-K lines expected from the CX process in the starburst galaxy for the first time. Based on the image analysis, we have analyzed the RGS data extracted from the compact peak ($\sim 2'$) in the south outflow and detected a high forbidden-to-resonance ratio in the O VII He α triplet as well as several emission lines enhanced in the CX process such as C V K γ , and N VII and O VIII Ly α . The RGS spectra of all observations are well fitted with the model that consists of three different plasma temperatures ($\sim 0.2 \text{ keV}$, $\sim 0.5 \text{ keV}$, and $\sim 0.9 \text{ keV}$) and CX components with an additional nonthermal component. The CX emission accounts for $\sim 50\%$, $\sim 30\%$, $\sim 60\%$, $\sim 40\%$, and $\sim 30\%$ of the total flux of C VI, N VII, O VII f , O VII r , and O VIII Ly α lines, respectively, although the CX contributions to the emission lines of Ne and Mg are less than $\sim 10\%$. Including this CX emission component primarily affects the measured abundance measurement of these light elements in the thermal plasma components, tending towards lower values relative to earlier calculations. The temperature of the plasma as electron receiver in the CX process is significantly lower than the plasma components that emit most of X-rays. From the low temperature and an estimation of the CX emitting volume, the CX primarily occurs in a thin region near the

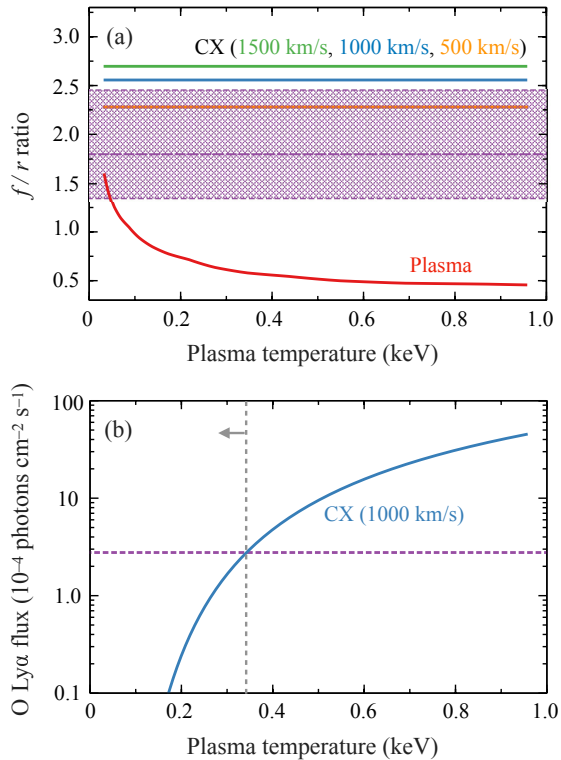


Figure 4. Comparison between the observational and theoretical (a) O VII f/r ratio and (b) O VIII Ly α flux. The purple area (line) indicates the observed line ratio (flux). The red curves in panel (a) is the ratio predicted from collisional ionization equilibrium plasma as a function of the plasma temperature. The orange, green, and blue curves shows the ratios in the CX cases of $v_{\text{col}} = 500$ km/s, 1000 km/s, and 1500 km/s, respectively. In panel (b), because three curves completely overlap each other, we only plot the case of $v_{\text{col}} = 1000$ km/s. The gray dot line and arrow represent the constrained upper limit of $kT_{e,\text{CX}} = 0.35$ keV.

interface of the plasma and gas whose temperature rapidly decreases due to thermal conduction.

We deeply appreciate all the *XMM-Newton* and HST members. We are also grateful to Drs. John C. Raymond and Q. Daniel Wang for helpful discussion and Dr. Caroline Huang for analysis of HST data. H.O. is supported by Japan Society for the Pro-motion of Science (JSPS) Research Fellowship for Research Abroad.

APPENDIX

A. ESTIMATION OF V_{CX}

The CX volume V_{CX} can be estimated from the emission measure of the CX component VEM_{CX} , defined as $\int n_{(\text{H+He})}^d n_{\text{H}}^r dV_{\text{CX}}$, where $n_{(\text{H+He})}^d$ and n_{H}^r are the total density of neutral hydrogen and helium of the donor gas and the hydrogen density of the receiver plasma, respectively. The average VEM_{CX} is estimated to be $0.9 \times 10^{57} \text{ cm}^{-3}$ by applying Equation 1 to values in Table 2. In order to calculate V_{CX} , we need to obtain $n_{(\text{H+He})}^d$ and n_{H}^r . According to Shopbell & Bland-Hawthorn (1998), $n_{(\text{H+He})}^d$ is $\sim 14 \text{ cm}^{-3}$ under the assumption of solar abundances of H and He. The n_{H}^r is given by the emission measure of the plasma components EM_{pl} , defined as $\int n_{\text{H}}^r n_e^r dV_{\text{pl}} \text{ cm}^{-3}$, where n_e^r is the electron density of the receiver plasma. Assuming the average $\text{VEM}_{\text{pl}} = \text{VEM}_{\text{cold}} + \text{VEM}_{\text{med}} + \text{VEM}_{\text{hot}} = 8.1 \times 10^{61} \text{ cm}^{-3}$, we can estimate n_{H}^r to be $\sim 0.018 \text{ cm}^{-3}$. Here, we have used the relation of $1.2 n_{\text{H}}^r \sim n_e^r$. Finally, we obtain V_{CX} to be $3.6 \times 10^{57} \text{ cm}^3$.

REFERENCES

- Arnaud, K. A. 1996, *Astronomical Data Analysis Software and Systems V*, 101, 17
- Bertone, S., Aguirre, A., & Schaye, J. 2013, *MNRAS*, 430, 3292. doi:10.1093/mnras/stt131
- Bobin, J., Rapin, J., Larue, A., et al. 2015, *IEEE Transactions on Signal Processing*, 63, 1199. doi:10.1109/TSP.2015.2391071
- Boogert, A. C. A., Gerakines, P. A., & Whittet, D. C. B. 2015, *ARA&A*, 53, 541. doi:10.1146/annurev-astro-082214-122348

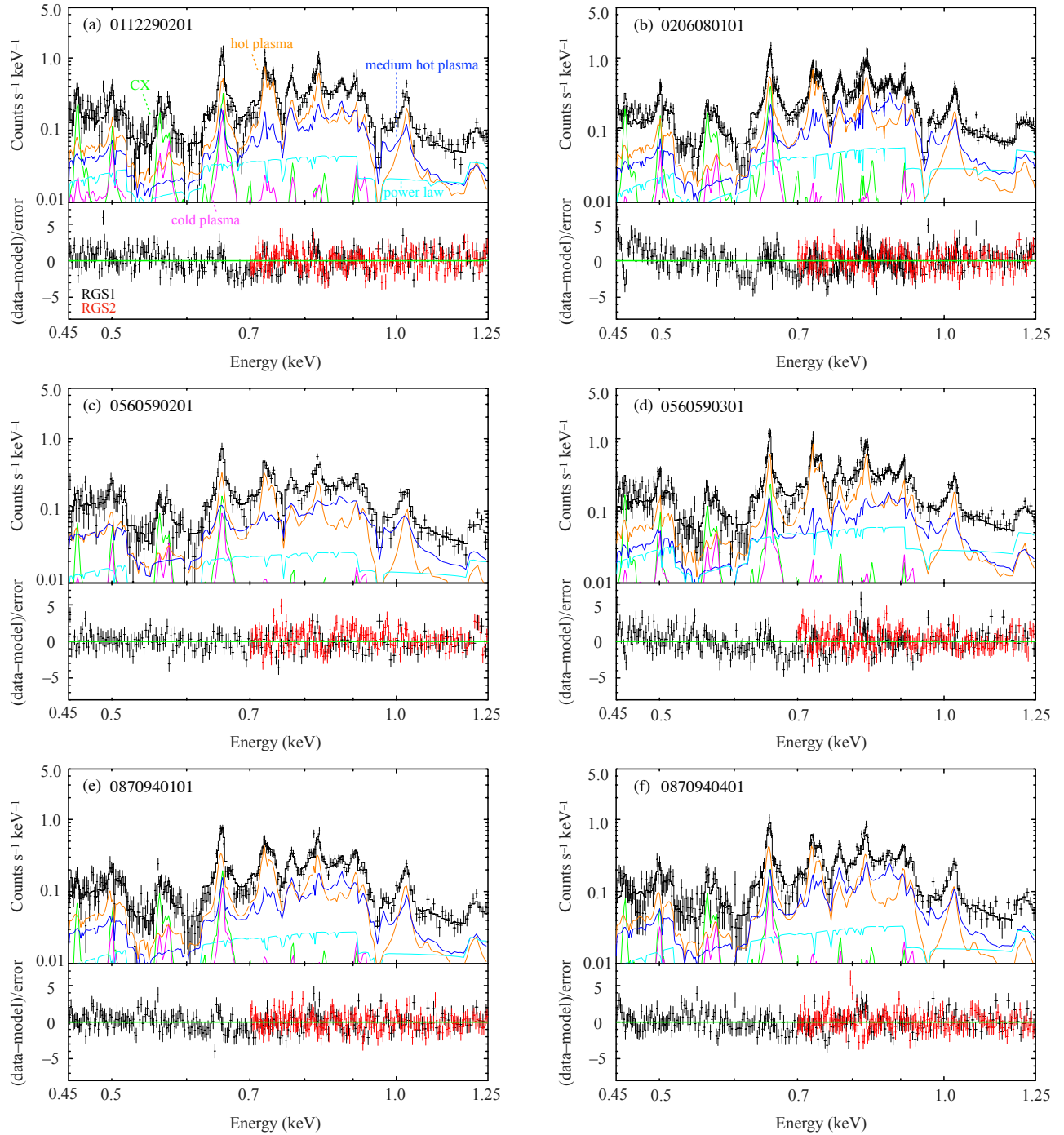


Figure 5. (a) RGS1+2 first- (black) and second-order (red) spectra of OBS.ID=0112290201 plotted with the best-fit model. The blue, magenta, orange, green, and black curves represent the CX model, the cold, medium hot, hot plasma models, and the sum of the models to RGS1+2 first-order data. (b)–(f) Same as panel (a) but for OBS. ID=0206080101, 0206080101, 0560590201, 0560590301, 0870940101, and 0870940101.

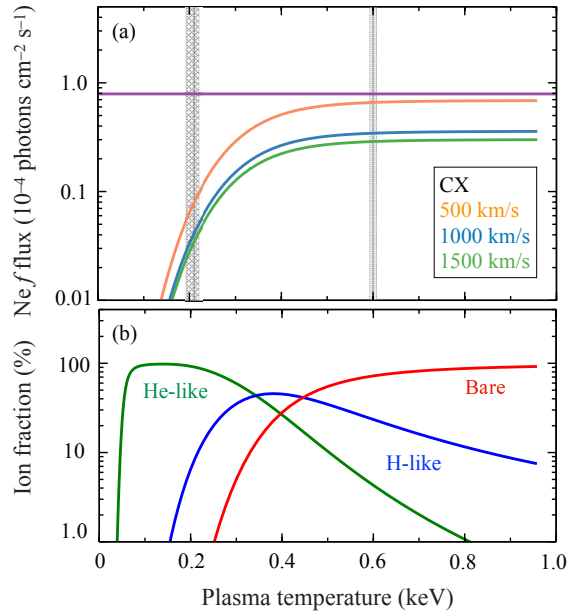


Figure 6. (a) Comparison between the observational Ne VII f flux (purple) and that theoretically expected in the CX process with $v_{\text{col}} = 500$ km/s (orange), 1000 km/s (blue), and 1500 km/s (green), respectively. The gray hatched (~ 0.2 keV) and filled (~ 0.6 keV) areas correspond to the constrained $kT_{e,\text{CX}}$ range in our results and in Zhang et al. (2014), respectively. (b) Ion fraction of Ne in the He-like (green), H-like (blue), and bare state (red) as a function of the plasma temperature.

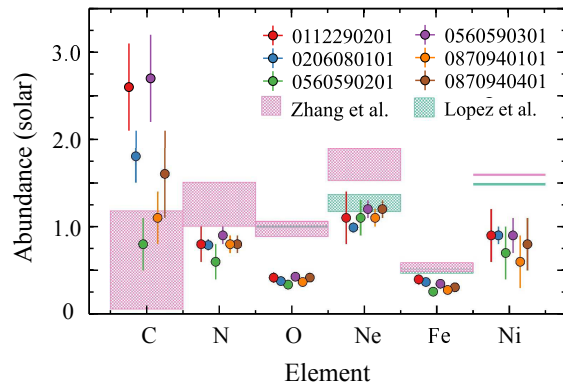


Figure 7. Elemental abundances relative to the solar values of Wilms et al. (2000). The magenta and light green hatched areas correspond to previous measurements in Zhang et al. (2014) and Region S1 by Lopez et al. (2020), that are also normalized by the solar abundances of Wilms et al. (2000) and plotted for comparison.

Borthakur, S., Heckman, T., Strickland, D., et al. 2013, ApJ, 768, 18. doi:10.1088/0004-637X/768/1/18

Bland-Hawthorn, J., Veilleux, S., & Cecil, G. 2007, Ap&SS, 311, 87. doi:10.1007/s10509-007-9567-8

Cash, W. 1979, ApJ, 228, 939. doi:10.1086/156922

Chevalier, R. A. & Clegg, A. W. 1985, Nature, 317, 44. doi:10.1038/317044a0

Cooper, J. L., Bicknell, G. V., Sutherland, R. S., et al. 2008, ApJ, 674, 157. doi:10.1086/524918

Cumbee, R. S., Mullen, P. D., Lyons, D., et al. 2018, ApJ, 852, 7. doi:10.3847/1538-4357/aa99d8

Das, S., Mathur, S., Nicastro, F., et al. 2019, ApJL, 882, L23. doi:10.3847/2041-8213/ab3b09

Dickey, J. M. & Lockman, F. J. 1990, ARA&A, 28, 215. doi:10.1146/annurev.aa.28.090190.001243

Freedman, W. L., Hughes, S. M., Madore, B. F., et al. 1994, ApJ, 427, 628. doi:10.1086/174172

Herwig, F. 2005, ARA&A, 43, 435.

doi:10.1146/annurev.astro.43.072103.150600

Hitomi Collaboration, Aharonian, F., Akamatsu, H., et al. 2018, PASJ, 70, 10. doi:10.1093/pasj/psx127

Hoopes, C. G., Heckman, T. M., Strickland, D. K., et al. 2005, ApJL, 619, L99. doi:10.1086/423032

Konami, S., Matsushita, K., Tsuru, T. G., et al. 2011, PASJ, 63, S913. doi:10.1093/pasj/63.sp3.S913

Kuntz, K. D. & Snowden, S. L. 2008, A&A, 478, 575.

doi:10.1051/0004-6361:20077912

Lallement, R. 2004, A&A, 422, 391.

doi:10.1051/0004-6361:20035625

Lehnert, M. D., Heckman, T. M., & Weaver, K. A. 1999, ApJ, 523, 575. doi:10.1086/307762

Liu, J., Mao, S., & Wang, Q. D. 2011, MNRAS, 415, L64.

doi:10.1111/j.1745-3933.2011.01079.x

Liu, J., Wang, Q. D., & Mao, S. 2012, MNRAS, 420, 3389.

doi:10.1111/j.1365-2966.2011.20263.x

Lopez, L. A., Mathur, S., Nguyen, D. D., et al. 2020, ApJ, 904, 152. doi:10.3847/1538-4357/abc010

McKeith, C. D., Greve, A., Downes, D., et al. 1995, A&A, 293, 703

Melioli, C., de Gouveia Dal Pino, E. M., & Geraissate, F. G. 2013, MNRAS, 430, 3235. doi:10.1093/mnras/stt126

Mullen, P. D., Cumbee, R. S., Lyons, D., et al. 2016, ApJS, 224, 31. doi:10.3847/0067-0049/224/2/31

Mullen, P. D., Cumbee, R. S., Lyons, D., et al. 2017, ApJ, 844, 7. doi:10.3847/1538-4357/aa7752

Müller-Sánchez, F., Prieto, M. A., Mezcuca, M., et al. 2013, ApJL, 763, L1. doi:10.1088/2041-8205/763/1/L1

Mutchler, M., Bond, H. E., Christian, C. A., et al. 2007, PASP, 119, 1. doi:10.1086/511160

Nomoto, K., Tominaga, N., Umeda, H., et al. 2006, NuPhA, 777, 424. doi:10.1016/j.nuclphysa.2006.05.008

Ohyama, Y., Taniguchi, Y., Iye, M., et al. 2002, PASJ, 54, 891. doi:10.1093/pasj/54.6.891

Okon, H., Tanaka, T., Uchida, H., et al. 2020, ApJ, 890, 62. doi:10.3847/1538-4357/ab6987

Okon, H., Tanaka, T., Uchida, H., et al. 2021, ApJ, 921, 99. doi:10.3847/1538-4357/ac1e2c

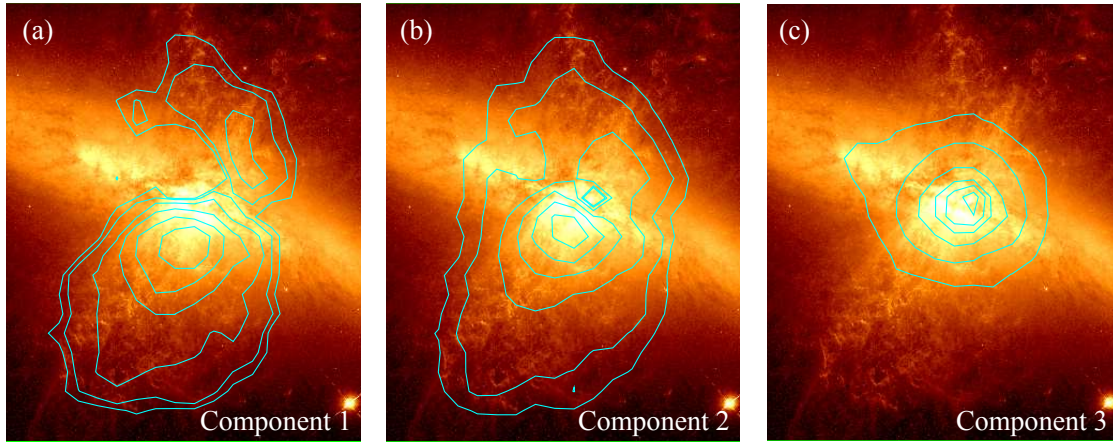


Figure 8. $H\alpha$ band image (F658N) taken with ACS onboard HST (Mutchler et al. 2007). The cyan contours in the panels (a), (b), and (c) indicate the counts maps of the components 1, 2, and 3 in Figure 1(b), respectively

- Oppenheimer, B. D. & Davé, R. 2006, *MNRAS*, 373, 1265.
doi:10.1111/j.1365-2966.2006.10989.x
- Origlia, L., Ranalli, P., Comastri, A., et al. 2004, *ApJ*, 606, 862.
doi:10.1086/383018
- Peeples, M. S. & Shankar, F. 2011, *MNRAS*, 417, 2962.
doi:10.1111/j.1365-2966.2011.19456.x
- Picquenot, A., Acero, F., Bobin, J., et al. 2019, *A&A*, 627, A139.
doi:10.1051/0004-6361/201834933
- Picquenot, A., Acero, F., Holland-Ashford, T., et al. 2021, *A&A*, 646, A82. doi:10.1051/0004-6361/202039170
- Ranalli, P., Comastri, A., Origlia, L., et al. 2008, *MNRAS*, 386, 1464. doi:10.1111/j.1365-2966.2008.13128.x
- Rubin, K. H. R., Prochaska, J. X., Koo, D. C., et al. 2014, *ApJ*, 794, 156. doi:10.1088/0004-637X/794/2/156
- Rupke, D. 2018, *Galaxies*, 6, 138. doi:10.3390/galaxies6040138
- Salak, D., Nakai, N., Miyamoto, Y., et al. 2013, *PASJ*, 65, 66.
doi:10.1093/pasj/65.3.66
- Savage, B. D. & Sembach, K. R. 1996, *ARA&A*, 34, 279.
doi:10.1146/annurev.astro.34.1.279
- Schneider, E. E., Ostriker, E. C., Robertson, B. E., et al. 2020, *ApJ*, 895, 43. doi:10.3847/1538-4357/ab8ae8
- Sharp, R. G. & Bland-Hawthorn, J. 2010, *ApJ*, 711, 818.
doi:10.1088/0004-637X/711/2/818
- Shopbell, P. L. & Bland-Hawthorn, J. 1998, *ApJ*, 493, 129.
doi:10.1086/305108
- Strickland, D. K., Heckman, T. M., Weaver, K. A., et al. 2000, *AJ*, 120, 2965. doi:10.1086/316846
- Smith, R. K., Odaka, H., Audard, M., et al. 2014, arXiv:1412.1172.
doi:10.48550/arXiv.1412.1172
- Strickland, D. K. & Heckman, T. M. 2009, *ApJ*, 697, 2030.
doi:10.1088/0004-637X/697/2/2030
- Suzuki, H., Yamaguchi, H., Ishida, M., et al. 2020, *ApJ*, 900, 39.
doi:10.3847/1538-4357/aba524
- Todini, P. & Ferrara, A. 2001, *MNRAS*, 325, 726.
doi:10.1046/j.1365-8711.2001.04486.x
- Tsuru, T. G., Ozawa, M., Hyodo, Y., et al. 2007, *PASJ*, 59, 269.
doi:10.1093/pasj/59.sp1.S269
- Veilleux, S., Cecil, G., & Bland-Hawthorn, J. 2005, *ARA&A*, 43, 769. doi:10.1146/annurev.astro.43.072103.150610
- Walter, F., Weiss, A., & Scoville, N. 2002, *ApJL*, 580, L21.
doi:10.1086/345287
- Watson, M. G., Stanger, V., & Griffiths, R. E. 1984, *ApJ*, 286, 144.
doi:10.1086/162583
- Werk, J. K., Prochaska, J. X., Cantalupo, S., et al. 2016, *ApJ*, 833, 54. doi:10.3847/1538-4357/833/1/54
- Wilms, J., Allen, A., & McCray, R. 2000, *ApJ*, 542, 914.
doi:10.1086/317016
- Wise, M. W. & Sarazin, C. L. 1989, *ApJ*, 345, 384.
doi:10.1086/167913
- Wu, K., Li, K. J., Owen, E. R., et al. 2020, *MNRAS*, 491, 5621.
doi:10.1093/mnras/stz3301
- Zhang, S., Wang, Q. D., Ji, L., et al. 2014, *ApJ*, 794, 61.
doi:10.1088/0004-637X/794/1/61